

# Contribution of Phosphorus and Sulfur on Hot Cracking Susceptibility for Extra-High-Purity 25Cr-35Ni Stainless Steels

*In this research, the hot cracking behavior of extra-high-purity 25Cr-35Ni steel was investigated, and quantitative influences of minor and impurity elements on the hot cracking susceptibility were clarified*

BY K. SAIDA, Y. NISHIJIMA, K. NISHIMOTO, K. KIUCHI, AND J. NAKAYAMA

## ABSTRACT

The hot cracking susceptibility of extra-high-purity 25Cr-35Ni stainless steel was evaluated by the transverse-Varestraint test while varying the contents of phosphorus (P) and sulfur (S). The solidification and ductility-dip cracking susceptibilities increased with an increase in the P and S contents in steels. There was a good linear relationship between the compositional parameter ( $P + 1.22 S$ ) and ductility-dip temperature range as well as between ( $P + 1.19 S$ ) and the solidification brittle temperature range in extra-high-purity 25Cr-35Ni steel welds. The amount of  $P + 1.22 S$  in steels should be limited to approximately 90 ppm to obtain a sufficiently low ductility-dip cracking susceptibility in such welds. Numerical simulation of segregation behaviors for P and S revealed that they were segregated at grain boundaries in the ductility-dip temperature range during welding. A molecular orbital analysis suggested that ductility-dip cracking could be attributed to grain boundary embrittlement due to grain boundary segregation of P and S. The solidification and ductility-dip cracking susceptibilities could be improved by adding 20–70 ppm lanthanum (La) to extra-high-purity 25Cr-35Ni steel containing 6–8 ppm P and S. The ductility-dip cracking susceptibility decreased as a result of the desegregation of P and S to grain boundaries due to the scavenging effect of La.

extra-high-purity 25 mass-% Cr – 20 mass-% Ni (Type 310 stainless steel) and 25 mass-% Cr – 35 mass-% Ni steels, which are manufactured by the cold crucible induction melting (CCIM) with electron beam cold hearth refining (EB-CHR) methods (Ref. 3), have been proposed as candidates for corrosion-resistant alloys in the next generation of reprocessing facilities. In these extra-high-purity stainless steels, the total sum content of minor and impurity elements, such as carbon (C), oxygen (O), nitrogen (N), P, and S, can be reduced to less than 100 ppm. To practically apply such extra-high-purity stainless steels, these steels should also possess a superior and reliable weldability for fusion welding.

It is well known that austenitic stainless steels, especially fully austenitic stainless steels such as Type 310, are potentially susceptible to weld cracking (hot cracking). According to a previous study (Ref. 4), extra-high-purity stainless steel (Type 310EHP) has a negligible susceptibility to solidification cracking despite being a fully austenitic stainless steel (i.e., not containing any  $\delta$  ferrite). Consequently, refining to an extra-high-purity grade (purification) would be one of the most innovative countermeasures for solving the hot cracking issue of fully austenitic alloys such as those that are stainless steel and Ni based.

On the other hand, more corrosion-resistant (anti-intergranular corrosion) alloys are being developed for application in more severe corrosive environments found in spent nuclear fuel reprocessing facilities. A high-chromium (Cr) and high-Ni austenitic stainless steel is one of the most promising of these highly corrosion-resistant alloys. For instance, extra-high-purity 25 mass-% Cr – 35 mass-% Ni stainless steel, whose alloying composition is comparable to Alloy 800 (Incoloy® 800) as well as a Ni-based alloy with 30 mass-% Cr – 8 mass-% W – 2 mass-% Si grade have been recently developed as anti-intergran-

## Introduction

Spent nuclear fuel reprocessing facilities need to be constructed from materials offering high performance and reliability, ones that in particular have a high corrosion resistance to nitric acid. Therefore, nitric acid-resistant stainless steel grades having ultralow-carbon (ULC) contents, such as Types 304ULC and 316ULC, are currently used for the main components of reprocessing plants (Ref. 1). However, it has been found that intergranular corro-

sion occurred in devices in the reprocessing line after a short period of test operation. To improve intergranular corrosion resistance, there is an urgent demand that these materials be replaced with ones with improved intergranular corrosion resistance, making them more resistant to such an environment.

Recently, highly pure corrosion-resistant stainless steels containing a large amount of nickel (Ni) have been developed as nitric acid-proof alloys to replace existing Types 304ULC and 316ULC stainless steels (Ref. 2). For example,

K. SAIDA (saida@mapse.eng.osaka-u.ac.jp), Dr. Eng., is a professor in the Division of Materials & Manufacturing Science, Graduate School of Engineering, Osaka University. Y. NISHIJIMA is a graduate student in the Division of Materials & Manufacturing Science, Graduate School of Engineering, Osaka University. K. NISHIMOTO, Dr. Eng., is a professor in the Department of the Application of Nuclear Technology, Fukui University of Technology. K. KIUCHI is with the Nuclear Science and Energy Directorate, Japan Atomic Energy Agency. J. NAKAYAMA is with the Natural Resources & Engineering Business, Kobe Steel, Ltd.

## KEYWORDS

Extra-High Purity  
25Cr-35Ni Stainless Steel  
Hot Cracking Susceptibility  
Hot Ductility  
Grain Boundary Segregation  
Molecular Orbital Analysis  
Lanthanum Addition  
Scavenging Effect

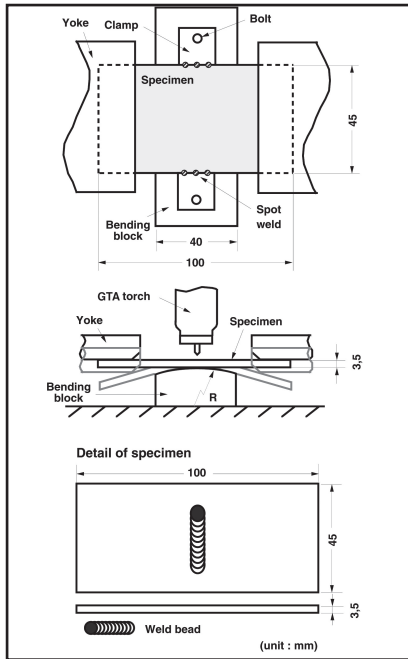


Fig. 1 — Schematic illustration of the transverse-Varestraint test procedure.

ular corrosion alloys (Ref. 3). Among those alloys, extra-high-purity 25 mass-% Cr – 35 mass-% Ni stainless steel, which is also manufactured by a combination of CCIM with EB-CHR methods as described previously, possesses a fully austenitic microstructure as well as higher Cr and Ni contents compared with conventional stainless steels. Therefore, there is fear that such steel is potentially susceptible to hot cracking, even if refined to extra-high-purity grade.

A great number of studies have been performed concerning the hot cracking behavior of fully austenitic stainless steels. According to these studies, controversial hot cracking in such steels would be dominantly regarded as solidification cracking (fusion zone cracking) and liquation cracking (HAZ cracking and/or weld metal HAZ cracking). As for the solidification cracking susceptibility in fully austenitic stainless steels, impurity elements such as P and S greatly influenced solidification cracking susceptibility (Refs. 5–9), and the (P + S)

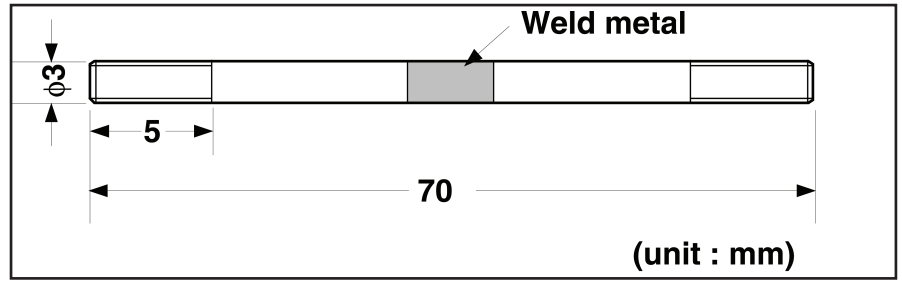


Fig. 2 — Dimensions of the specimen for evaluating hot ductility by the Gleeble® test.

content should be reduced to less than 0.01 mass-% to obtain excellent crack resistance in the practical use of Type 310 stainless steel (Ref. 5). Furthermore, several researchers reported that the quantitative influence of P on solidification cracking was comparable to or larger than (1.1–2.1 times) that of S in Types 304 and 310S stainless steels (Refs. 5–8), while other researchers conversely suggested that S was more harmful in solidification cracking compared with P in austenitic stainless steels (Type 308) (Ref. 9).

As for the liquation cracking in fully austenitic stainless steels, P and S also greatly influenced liquation cracking susceptibility (Refs. 6, 9–12). However, the effects of P and S on liquation cracking would be slightly different from that on solidification cracking. For instance, S was more potent in exacerbating liquation cracking than P (P + S level of 0.032%) (Ref. 12). Meanwhile, it has been also reported that the minor and impurity elements such as P, S, C, and boron (B), also affected the hot cracking susceptibility of high-Cr and high-Ni stainless steels such as Alloy 800 (Refs. 13–15). However, these previous investigations covered the hot cracking susceptibility of commercial purity stainless steels containing some amounts of C, P, and S as well as manganese (Mn) and silicon (Si). Therefore, the characteristic influence and quantitative contribution of minor and impurity elements to the hot cracking behavior in austenitic stainless steels are still unclear.

On the other hand, the authors have already reported that the solidification crack-

ing susceptibility of Type 310 stainless steels drastically decreased as the amounts of minor and impurity elements were reduced (purification), while the ductility-dip cracking susceptibility slightly increased in extra-high-purity steel (Ref. 4). In addition, the ductility-dip cracking susceptibility generally tends to heighten in the high-Cr and high-Ni alloys. Accordingly, there is a possibility that 25 mass-% Cr – 35 mass-% Ni extra-high-purity stainless steel would be more susceptible to ductility-dip cracking than solidification cracking.

The objective of this study is to evaluate the weldability of extra-high-purity corrosion-resistant stainless steels. In the present report, the cracking behavior of an anti-intergranular corrosion extra-high-purity 25 mass-% Cr – 35 mass-% Ni stainless steel is investigated, and the quantitative influences of minor and impurity elements on hot cracking susceptibility are clarified. The mechanism of action for steel refinement to change the hot cracking susceptibility is discussed based on a numerical analysis of grain boundary segregation and grain boundary embrittlement in the weld metal. Furthermore, the effect of the rare earth metal (REM), La, as an addition to the steel is investigated to further improve the hot cracking susceptibility of extra-high-purity stainless steels.

## Materials and Experimental Procedures

### Materials

Eight types of extra-high-purity 25

Table 1 — Chemical Compositions of Materials Used (mass-%)

Steel	C	Si	Mn	P	S	Ni	Cr	Ti	O	N	La
U21	0.0059	<0.01	<0.01	0.0005	0.0001	34.76	26.14	0.15	0.0008	0.0013	—
U22	0.0038	<0.01	<0.01	0.0004	0.0032	35.81	26.22	0.11	0.0038	0.0033	—
U23	0.0042	<0.01	<0.01	0.0004	0.0092	34.36	25.98	0.12	0.0044	0.0036	—
U24	0.0008	<0.01	<0.01	0.0036	0.0009	35.05	22.89	0.20	0.0011	0.0009	—
U25	0.0014	<0.01	<0.01	0.0110	0.0008	35.85	22.73	0.21	0.0007	0.0009	—
U26	0.0038	<0.01	<0.01	0.0005	0.0003	35.82	25.78	0.12	0.0052	0.0041	0.003
U27	0.0180	<0.01	<0.01	0.0004	0.0003	35.39	25.92	0.14	0.0045	0.0049	0.008
U28	0.0036	<0.01	<0.01	0.0003	0.0003	35.12	25.71	0.13	0.0036	0.0043	0.021

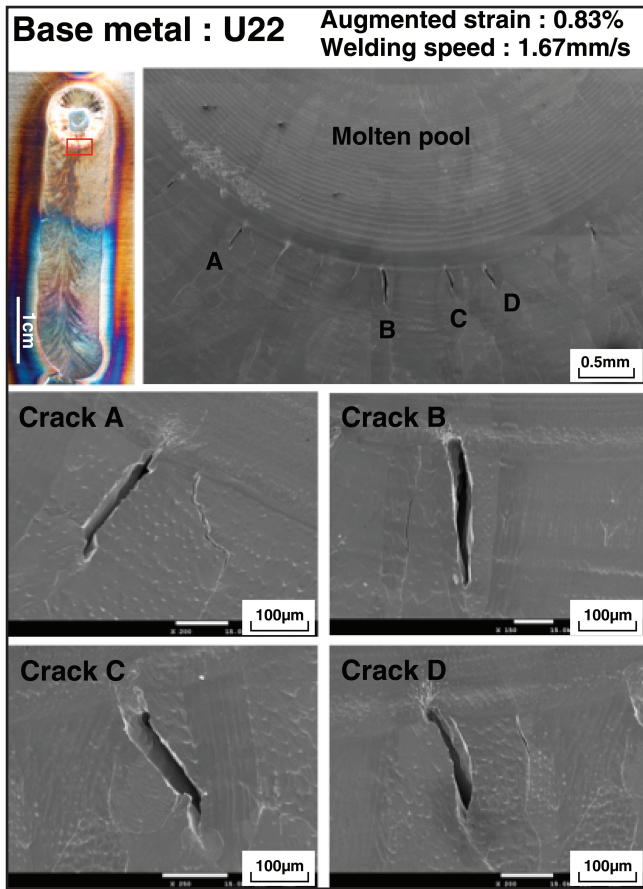


Fig. 3 — Appearance of hot cracks after the transverse-Varestraint test.

mass-% Cr – 35 mass-% Ni stainless steels (hereinafter referred to as 25Cr-35Ni steel) with various amounts of minor and impurity elements, such as P, S, and La, were used for the base metal. Table 1 shows the chemical compositions of the base metals used in this study. The contents of C, Si, and Mn in the extra-high-purity 25Cr-35Ni steels are greatly reduced compared to those of other conventional stainless steels (to refine the impurity elements, a very small amount of titanium [Ti] is present).

#### Experimental Procedures

The hot cracking susceptibility of the steels was evaluated by the transverse-Varestraint test as shown in Fig. 1. The augmented strain was varied between 0.075 and 0.83% (the maximum augmented strain was determined based on the condition of the crack length being saturated (Ref. 16)). The transverse-welding (GTAW) condition was as follows: arc current, 150 A; arc voltage, 14 V; and welding speed, 1.67 mm/s. The specimens varied from 3 to 5 mm thick. The temperature distribution behind the molten pool in the weld bead was measured with a thermocouple during welding to obtain the crack-

ing temperature range. The crack surface occurring in the Varestraint test was observed using a scanning electron microscope (SEM). The hot ductility (reduction of area) of the weld metal was evaluated via the Gleeble test at 873–1573 K applying a crosshead speed of 6 mm/s.

The dimensions of the specimen for the Gleeble test are shown in Fig. 2.

#### Hot Cracking Susceptibility Evaluated by Transverse-Varestraint Test

The characteristic contribution of P and S on the hot cracking susceptibility was investigated using extra-high-purity 25Cr-35Ni steels (fully austenitic stainless steels) in the present study.

#### Hot Cracking Behavior

An example of hot cracks occurring in a transverse-Varestraint test of a particular extra-high-purity 25Cr-35Ni steel is shown in Fig. 3 (specimen U22, augmented strain 0.83%). Cracks occurring in

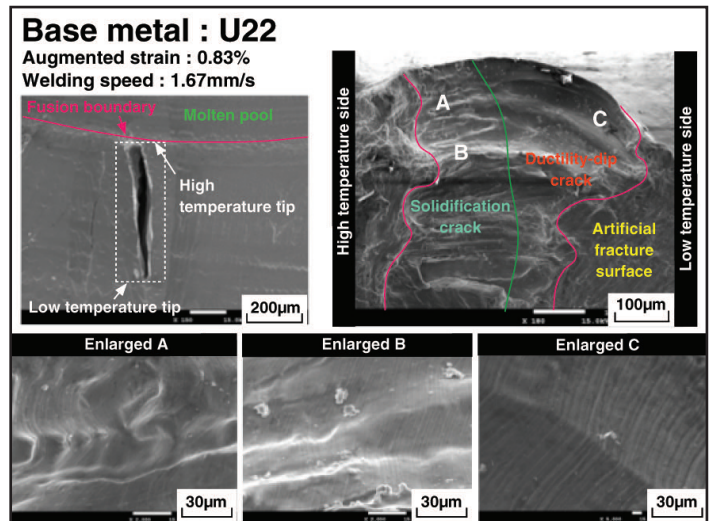


Fig. 4 — SEM microstructure of crack and crack surface in weld metal U22 after transverse-Varestraint testing.

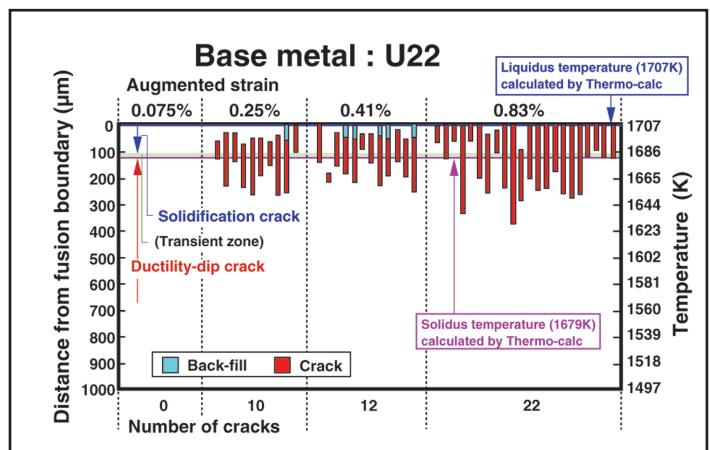


Fig. 5 — Location and temperature range of hot cracking in the weld metal U22.

the weld metal could be classified into two types — cracks occurring distant from the weld interface and those occurring adjacent to the weld interface. The microstructure of the crack surface occurring adjacent to the weld interface is shown in Fig. 4. Two characteristic morphologies were observed in the crack surface, namely, the crack surface on the high-temperature side (adjacent to the weld interface) had a dendritic structure with a trace of melting, while that on the low temperature side (distant from the weld interface) was an intergranular fracture (without melting) together with slip lines. The morphological features of the crack surface suggest that the former crack could be regarded as solidification cracking, while the latter was due to ductility-dip cracking. In addition, some regions, which have both morphological features, existed on one crack surface (called the “transient zone” (Ref. 4)).

The hot cracking behavior of an extra-high-purity 25Cr-35Ni steel (specimen U22) occurring in the transverse-Vare-

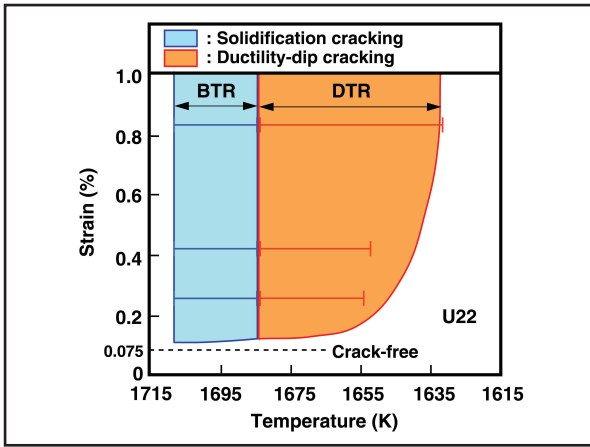


Fig. 6 — Strain-temperature curves for hot cracking in weld metal U22.

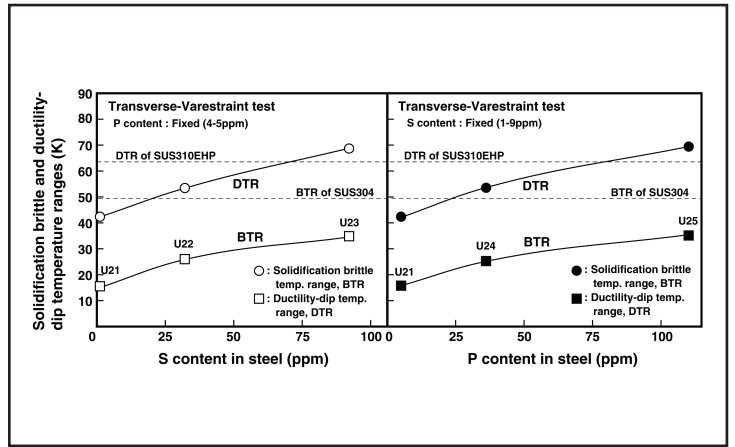


Fig. 7 — Effects of P and S contents in steel on solidification and ductility-dip cracking susceptibilities.

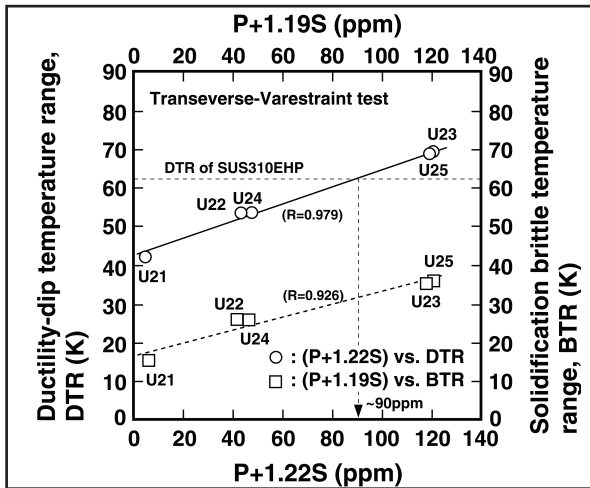


Fig. 8 — Regression analyses of solidification and ductility-dip cracking susceptibilities as functions of P and S contents.

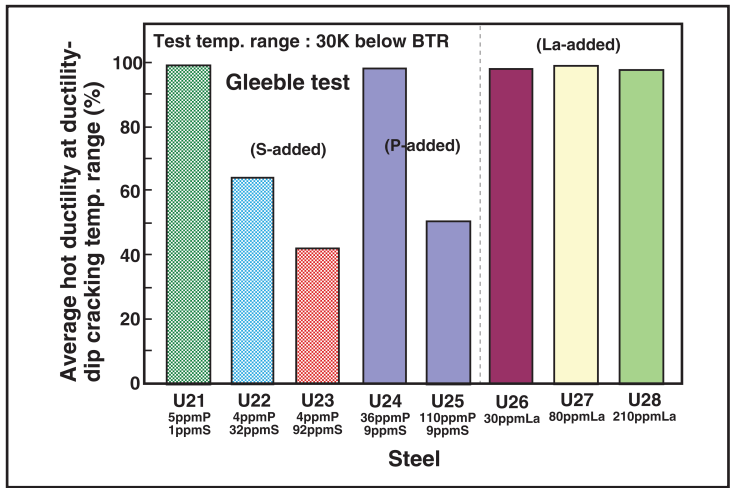


Fig. 9 — Average hot ductility of weld metals at the ductility-dip temperature range.

straint test is shown in Fig. 5. The location (distance from the weld interface) and length of each hot crack as well as the cracking temperature range are indicated in the figure. The distance from the weld interface was converted into temperature based on the temperature distribution behind the molten pool measured during the transverse-Varestraint testing. In addition, the total number of cracks and classification of hot cracking are also shown in the figure. Both solidification and ductility-dip cracks occurred in every augmented strain, and the total numbers of cracks and cracking temperature range increased with an increase in the augmented strain.

Figure 6 shows the strain-temperature curves for hot crack generation obtained from Fig. 5 (specimen U22). In this figure, the transient zone was approximately divided half into solidification and half into ductility-dip cracks. The solidification and ductility-dip cracking temperature ranges were expanded with an increase in the augmented strain at the lower strain; how-

ever, they saturated at an augmented strain of around 0.8%. Accordingly, the solidification brittle temperature range (BTR) and ductility-dip temperature range (DTR) were obtained as the saturated cracking temperature ranges shown in the figure.

#### Effects of P and S Contents on Hot Cracking Susceptibility

The solidification and ductility-dip cracking susceptibilities of the steels used were evaluated from the BTR and DTR, respectively. Figure 7 shows the effects of P and S contents in steels on the BTR and DTR. Not only the BTR but also the DTR increased with an increase in P and S contents. The BTRs of the steels remained at a sufficiently low level under the present experimental conditions (the BTRs of extra-high-purity 25Cr-35Ni steels were much lower than that of Type 304 stainless steel, which is negligibly susceptible to solidification cracking). However, their

DTRs exceeded that of Type 310EHP stainless steel (Ref. 4) when the P and S contents exceeded approximately 75 ppm.

It should be noted that there would likely not be a serious problem of ductility-dip cracking during practical welding (Ref. 4), just because the DTR level had slightly exceeded that of Type 310EHP. Figure 8 shows a regression analysis of the hot cracking susceptibility (BTR and DTR) against the P and S contents in the steel. The DTR of extra-high-purity 25Cr-35Ni steel could be expressed using the compositional parameter of  $P + 1.22S$ ; namely, S essentially enhanced the ductility-dip cracking susceptibility approximately 1.2 times as effectively as P. Furthermore, the amount of  $P + 1.22S$  in the steels should be limited to approximately 90 ppm to obtain a sufficiently low ductility-dip cracking susceptibility in 25Cr-35Ni stainless steel welds. Meanwhile, the BTR of extra-high-purity 25Cr-35Ni steel could be expressed using the compositional parameter of  $P + 1.19S$ ; namely, S

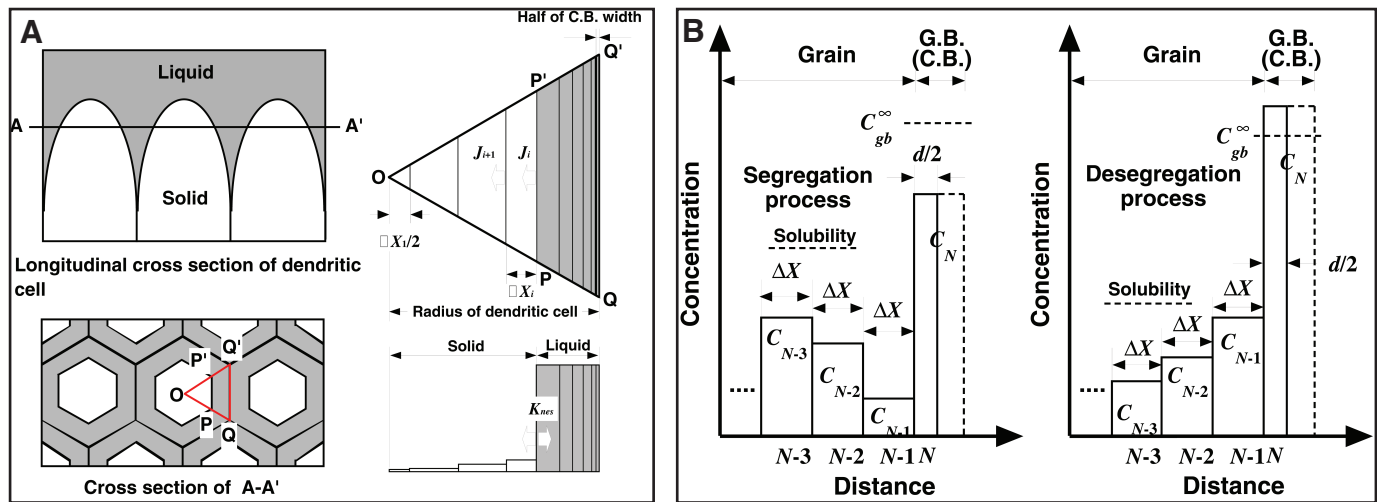


Fig. 10 — Schematic illustration of analysis mode of microsegregation during welding. A — Segregation during solidification; B — segregation and desegregation during cooling.

also enhanced the solidification cracking susceptibility approximately 1.2 times as effectively as P.

Although the results obtained here are qualitatively consistent with previous ones (Refs. 9, 10, 14), they might provide an important insight into the characteristic and quantitative contribution of P and S to the solidification and ductility-dip cracking

susceptibilities by employing extra-high-purity steels, where the effects of coexisting elements were negligible.

### Mechanism of Ductility-Dip Crack Generation in Extra-High-Purity Steels

As described previously, the solidifica-

tion cracking susceptibility of extra-high-purity 25Cr-35Ni steel was at a quite low level, and accordingly, the authors expect that the controversial hot cracking in it would, in fact, involve ductility-dip cracks. Hereinafter, the authors focus on the ductility-dip cracking, and discuss the mechanism of ductility-dip crack generation in extra-high-purity 25Cr-35Ni steels.

### Evaluation of Hot Ductility in Weld Metal

It has been recognized that the ductility-dip cracking susceptibility was closely related to the deformability of materials at an elevated temperature, and therefore, the hot ductility (reduction of area) of the weld metals was evaluated by the Gleeble test. Average values of the reduction of area for the weld metals within the ductility-dip cracking temperature range (from 30 K below the BTR to just below the BTR itself) are summarized in Fig. 9. The hot ductility decreased in the order of U21 > U22 > U23 or U21 ≈ U24 > U25; namely, it decreased with an increase in P and S contents in the steel (in addition, it has been confirmed that any fracture surfaces formed an intergranular fracture). It follows that the ductility-dip cracking susceptibility would heighten with a deterioration in the hot ductility.

Table 2 — Material Constants Used for Numerical Simulation of Grain Boundary Segregation Part A — Material Constants and Initial Conditions

Solute Element	P	S
Initial concentration (ppm)	4, 36, 110	0.76, 32, 92
Liquidus temp. (K)	1705	1705
Nonequilibrium distribution coefficient	$1.35 \times 10^{-2}$	$1.69 \times 10^{-2}$
Diffusion coefficient in liquid (m <sup>2</sup> /s), $D = D_0 \exp(-Q/RT)$	$D_0 = 4.70 \times 10^{-9}$ $Q = 33.6$ (kJ/mol)	$D_0 = 4.50 \times 10^{-9}$ $Q = 36$ (kJ/mol)
Diffusion coefficient in solid (m <sup>2</sup> /s), $D = D_0 \exp(-Q/RT)$	$D_0 = 8.70 \times 10^{-4}$ $Q = 273$ (kJ/mol)	$D_0 = 7.50 \times 10^{-4}$ $Q = 236$ (kJ/mol)
Diffusion coefficient of vacancy in solid (m <sup>2</sup> /s), $D = D_0 \exp(-Q/kT)$	$D_0 = 1.00 \times 10^{-4}$ $Q = 2.49$ (eV)	$D_0 = 1.00 \times 10^{-4}$ $Q = 250$ (eV)
Diffusion coefficient of complexes in solid (m <sup>2</sup> /s), $D = D_0 \exp(-Q/kT)$	$D_0 = 1.70 \times 10^{-5}$ $Q = 1.71$ (eV)	$D_0 = 1.40 \times 10^{-5}$ $Q = 2.70$ (eV)
Equilibrium concentration of vacancy, $C_v = K_{v0} \exp(-E_{vF}/kT)$	$K_{v0} = 4.5$ $E_{vF} = 1.47$ (eV)	$K_{v0} = 4.5$ $E_{vF} = 1.47$ (eV)
Equilibrium concentration of complexes at solute concentration $C_c$ , $C_c = K_c C_v C_s \exp(-E_{vcF}/kT)$	$K_c = 12.0$ $E_{vcF} = 0.41$ (eV)	$K_c = 12.0$ $E_{vcF} = 0.90$ (eV)
Segregation energy (J/mol)	$\Delta G^p_0 = 50500$	$\Delta G^s_0 = 75000$
Interaction parameter (J/mol)		-78300

Table 2 — Material Constants Used for Numerical Simulation of Grain Boundary Segregation. Part B — Analysis Conditions

Analysis Conditions	
Dendrite radius (μm)	10.0
Grain boundary width (nm)	1.0
Number of mesh division	100

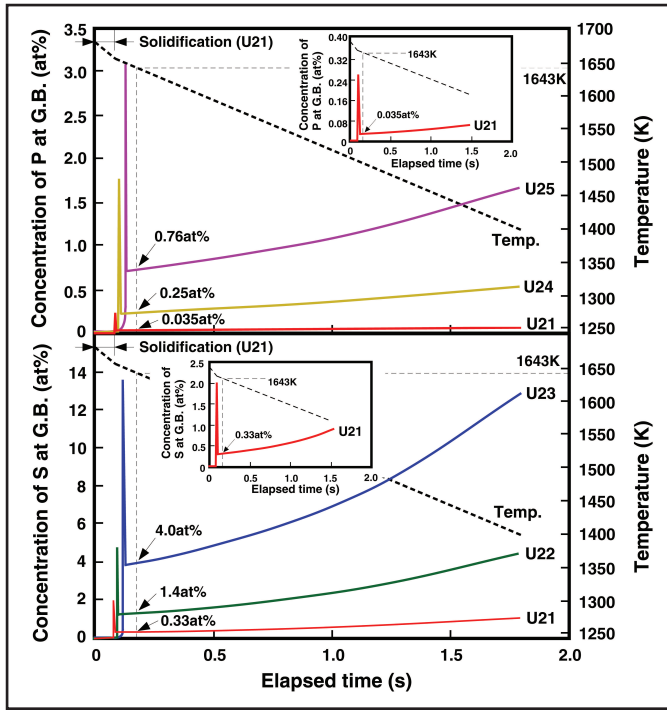


Fig. 11 — Calculated P and S concentrations at grain boundaries during cooling in welding.

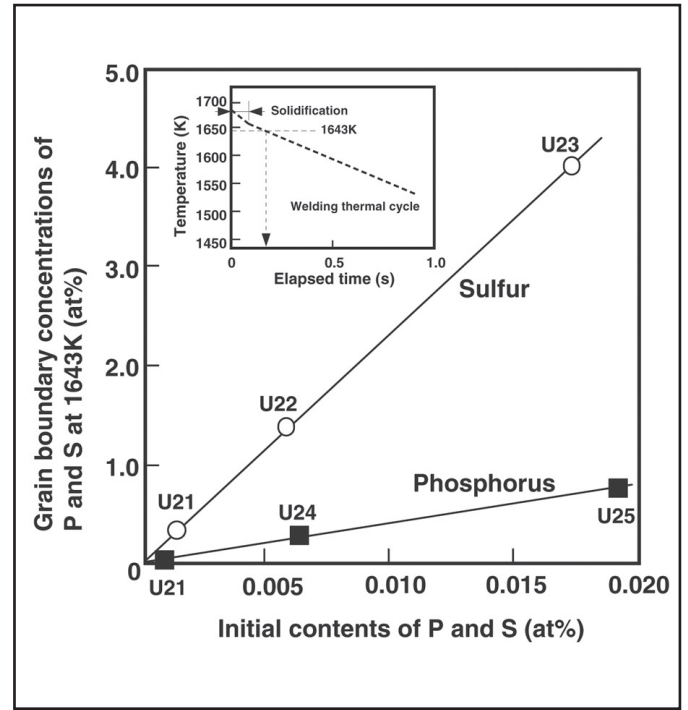


Fig. 12 — Relationship between initial contents and grain boundary concentrations at 1643 K of P and S.

### Numerical Analysis of Grain Boundary Segregation in Weld Metal

#### Analysis Model

To elucidate the deterioration mechanism of the hot ductility of extra-high-purity 25Cr-35Ni steels, grain boundary segregation of P and S in the weld metal was numerically analyzed. The present analysis model of microsegregation involves segregation during the solidification stage (Stage I) and segregation/desegregation during the cooling stage (Stage II) following solidification under the initial condition of an inhomogeneous distribution formed by solidification segregation (Ref. 16). To simplify the computation procedure, the solidification segregation behaviors of P and S to the cell boundary were calculated for pseudo-binary systems of (Fe – 25 mass-% Cr – 35 mass-% Ni) – P and (Fe – 25 mass-% Cr – 35 mass-% Ni) – S using the finite differential method (FDM) scheme. Furthermore, the cosegregation effect of P with S was considered in the nonequilibrium grain boundary segregation following solidification segregation using pseudo-ternary systems of (Fe – 25 mass-% Cr – 35 mass-% Ni) – P – S. The outline of the numerical models used in the present study is as follows:

#### 1. Solidification Segregation (Stage I)

The distribution of solutes in the solid phase during the solidification process was calculated by the nonequilibrium solidification segregation theory (Ref. 16). This

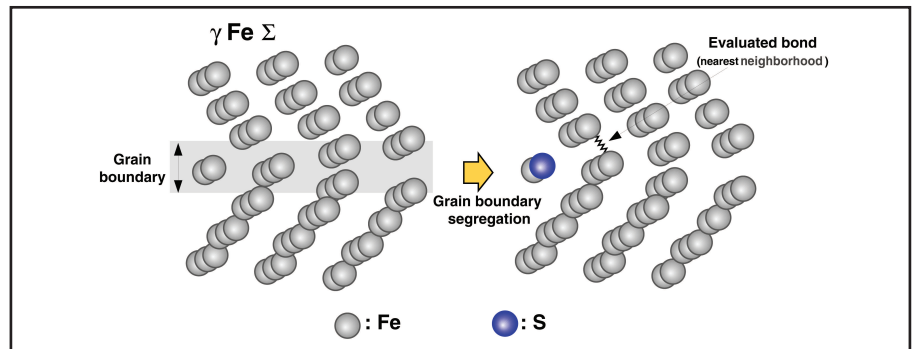


Fig. 13 — Schematic illustration of the cluster model used for molecular orbital analysis by the DV-Xα method.

employed a one-dimensional diffusion model in a regular triangle assuming that the morphology of a dendrite is basically a hexagonal prism, as shown in Fig. 10A. Symmetrical boundary conditions were applied to both end segments. The final segment of the liquid phase was defined as the final solidification boundary, the cell boundary (C.B.). The convection and diffusion in the liquid were ignored, while the diffusion in solid phase was allowed for analysis. The cosegregation effect of P with S was not considered in the solidification segregation process.

The diffusive flux  $J_i$  from a segment  $i$  to a segment  $i + 1$  is given by Fick's first law

$$J_i = D \frac{C_{i+1} - C_i}{\Delta x} \quad (1)$$

where  $D$  is the diffusion coefficient of solute,  $C_i$  and  $C_{i+1}$  are concentrations in segments  $i$  and  $i + 1$ , and  $\Delta x$  is a segment width. The change in solute concentration  $\Delta C_i$  during an infinitesimal time interval  $\Delta t$  at a segment  $i$  is expressed by

$$\frac{\Delta C_i}{\Delta t} \cdot \frac{S_i + S_{i-1}}{2} \cdot \Delta x_i = J_i S_i - J_{i-1} S_{i-1} \quad (2)$$

where  $S_i$  and  $S_{i-1}$  are sectional areas of segments  $i$  and  $i - 1$ . In the regular triangle model as shown in Fig. 10A,  $S_i$  is expressed by

$$S_i = \frac{1}{\sqrt{3}} \left( \sum_{k=1}^i \Delta x_k \right)^2 \quad (3)$$

where  $\Delta x_k$  is the segment width of segment  $k$ . From Equations 2 and 3,  $\Delta C_i$  is given by

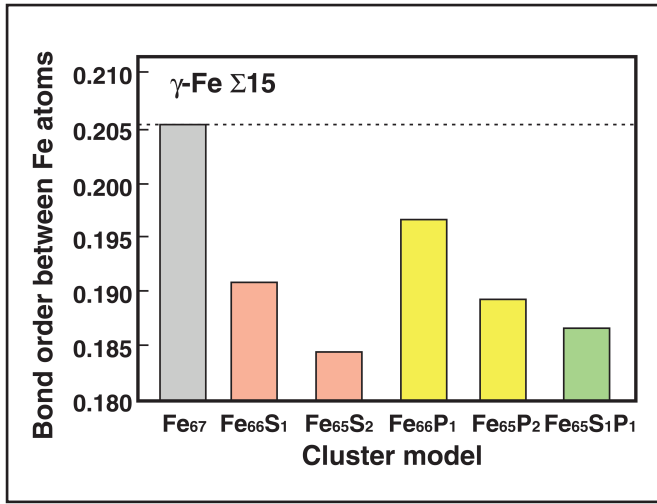


Fig. 14 — Calculated bond order between Fe atoms at the different grain boundary segregations of P and S.

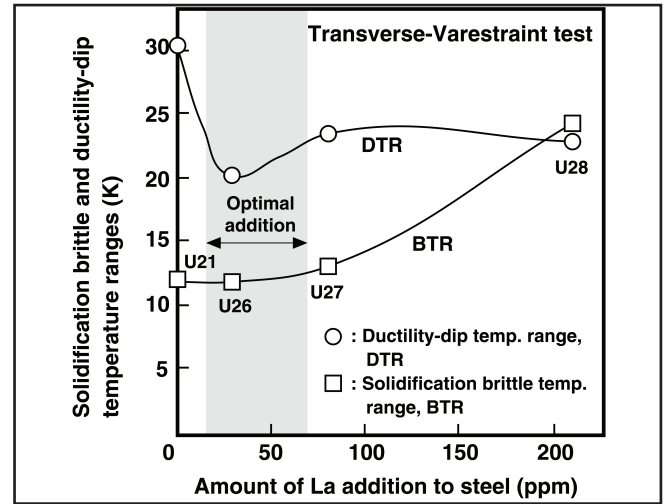


Fig. 15 — Effect of the amount of La addition on solidification and ductility-dip cracking susceptibilities.

$$\Delta C_i = \frac{2D\Delta t}{\Delta x_i(S_i + S_{i-1})} \left\{ S_i \frac{C_{i+1}^B - C_i^B}{\Delta x_i} - S_{i-1} \frac{C_i^B - C_{i-1}^B}{\Delta x_{i-1}} \right\} \quad (4)$$

where  $C_{i+1}^B$ ,  $C_i^B$ , and  $C_{i-1}^B$  are solute concentrations in segments  $i+1$ ,  $i$  and  $i-1$  at the previous  $\Delta t$  ( $\Delta t$  is a time step), respectively. Assuming the mass conservation law of solute in a dendrite holds, then Equation 5 becomes

$$\left( \sum_{k=1}^N \Delta x_k \right)^2 \cdot C_0 = \sum_{i=1}^N \left\{ \left( \sum_{k=1}^i \Delta x_k + \sum_{k=1}^{i-1} \Delta x_k \right) \cdot \Delta x_i \cdot C_i^S \right\} + \sum_{i=j+1}^N \left\{ \left( \sum_{k=1}^i \Delta x_k + \sum_{k=1}^{i-1} \Delta x_k \right) \cdot \Delta x_i \cdot C_i^L \right\} \quad (5)$$

where  $N$  is the total number of segments,  $C_0$  is the initial solute concentration,  $C_i^S$  is the solute concentration in solid phase segment  $i$ ,  $C_i^L$  is the solute concentration in liquid phase (assuming solute concentration in liquid phase being uniform), and  $j$  is a segment number of solid phase at the solid/liquid interface.

The solute concentration at the solid/liquid interface is given by the local equilibrium concept

$$C_j^S = K_{nes} C_{j+1}^L \quad (6)$$

where  $K_{nes}$  is the nonequilibrium distribution coefficient between solid and liquid

phases, and  $C_j^S$  and  $C_{j+1}^L$  are solute concentrations of solid and liquid phases at the solid/liquid interface, respectively. The nonequilibrium distribution coefficient can be represented by

$$K_{nes} = \frac{K_{es} + \varepsilon}{1 + \varepsilon}, \quad \varepsilon = R_v \frac{\lambda}{2D^L} \quad (7)$$

where  $K_{es}$  is the equilibrium distribution coefficient,  $\varepsilon$  is the Peclet number,  $R_v$  is the growth velocity of the dendrite (solidification rate),  $\lambda$  is the interatomic spacing, and  $D^L$  is the diffusion coefficient of the solute in a liquid. The solid/liquid interface migrates according to the solidification velocity determined by the cooling rate during solidification; in other words, the neighbor segment changes from the liquid to the solid phase.

## 2. Grain Boundary Cosegregation/Desegregation after Solidification (Stage II)

The distribution of solutes in the solid phase during the cooling process was calculated by the nonequilibrium cosegregation theory proposed by T. Xu (Ref. 17). According to the nonequilibrium grain boundary segregation theory, solute elements, atomic vacancies, and their complexes play roles in segregation, plus the segregated concentration at a grain boundary is determined by the diffusion of solute elements and complexes to a grain boundary during the segregation process. Meanwhile, during the desegregation process, by diffusion of solute elements into a grain as well as that of atomic vacancies to a grain boundary. The solute distribution present in grain boundary segregation was calculated based on a one-dimensional segregation model as shown in Fig. 10B. The final segment  $C_N$  was defined as the grain boundary (G.B.). The saturated solute concentration at the

grain boundary (equilibrium concentration)  $C_{GB}^\infty(t)$  of P and S during cosegregation at a temperature  $T$  and time  $t$  are given by

$$C_{GB,P}^\infty(t) = \frac{C_B^P \exp(\Delta G^P / RT)}{1 + C_B^P \exp(\Delta G^P / RT) + C_B^S \exp(\Delta G^S / RT)}$$

$$C_{GB,S}^\infty(t) = \frac{C_B^S \exp(\Delta G^S / RT)}{1 + C_B^P \exp(\Delta G^P / RT) + C_B^S \exp(\Delta G^S / RT)} \quad (8)$$

$$\Delta G^P = G_0^P + \beta C_N^S(t - \Delta t)$$

$$\Delta G^S = G_0^S + \beta C_N^P(t - \Delta t) \quad (9)$$

where  $C_B^P$  and  $C_B^S$  are the bulk concentrations of P and S,  $G_0^P$  and  $G_0^S$  are the segregation energies of P and S, respectively,  $\beta$  is the interaction parameter, and  $R$  is the gas constant. The solute concentrations of P and S at grain boundaries at time  $t$ ,  $C_N(t)$  are expressed by

$$\frac{C_N^P(t) - C_N^P(0)}{C_{GB,P}^\infty(t) - C_N^P(0)} = 1 - \exp\left(-\frac{4D_P \Delta t}{\alpha^P d}\right) \cdot \operatorname{erfc}\left(\frac{2\sqrt{D_P \Delta t}}{\alpha^P d}\right)$$

$$\frac{C_N^S(t) - C_N^S(0)}{C_{GB,S}^\infty(t) - C_N^S(0)} = 1 - \exp\left(-\frac{4D_S \Delta t}{\alpha^S d}\right) \cdot \operatorname{erfc}\left(\frac{2\sqrt{D_S \Delta t}}{\alpha^S d}\right) \quad (10)$$

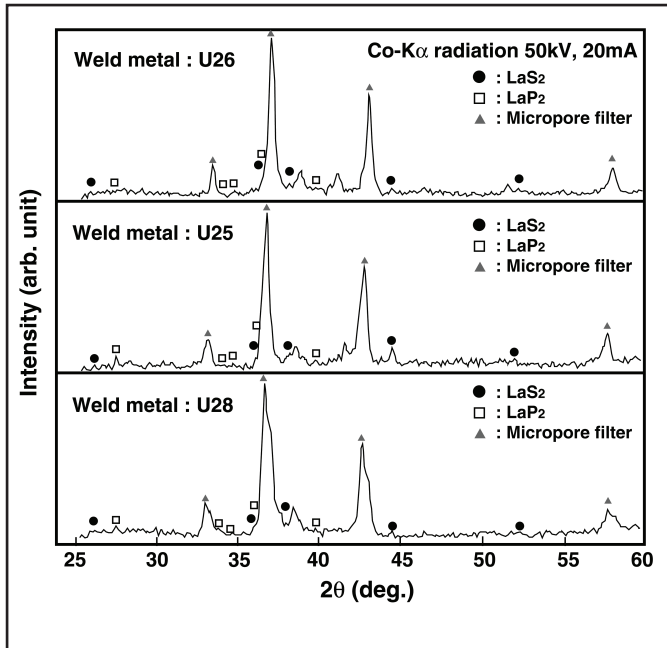


Fig. 16 — X-ray diffraction patterns of extracted residues from La-containing weld metals.

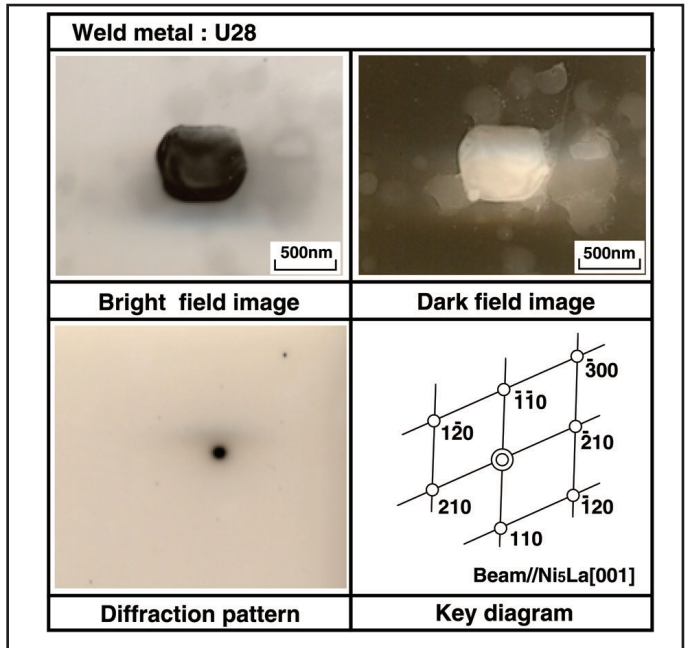


Fig. 17 — TEM microstructure and electron diffraction pattern of products in weld metal U28.

$$\alpha^P = C_{GB,P}^\infty(t)/C_B^P$$

$$\alpha^S = C_{GB,S}^\infty(t)/C_B^S \quad (11)$$

where  $C_N(0)$  is the initial concentration of solute,  $D_P$  and  $D_S$  are the diffusion coefficients of P and S in solid, respectively, and  $d$  is the grain boundary width. Consequently, the FDM scheme gives the change in solute concentrations of P and S at the grain boundary  $\Delta C_N(t)$

$$\Delta C_N^P(t) = \frac{2D_P \Delta t}{\Delta x_N \left( \sum_{k=1}^N \Delta x_k + \sum_{k=1}^{N-1} \Delta x_k \right)} \left\{ \sum_{k=1}^{N-1} \Delta x_k \cdot \frac{C_{GB,P}^\infty - C_N^{B,P}(t - \Delta t)}{\Delta x_N} \right\}$$

$$\Delta C_N^S(t) = \frac{2D_S \Delta t}{\Delta x_N \left( \sum_{k=1}^N \Delta x_k + \sum_{k=1}^{N-1} \Delta x_k \right)} \left\{ \sum_{k=1}^{N-1} \Delta x_k \cdot \frac{C_{GB,S}^\infty - C_N^{B,S}(t - \Delta t)}{\Delta x_N} \right\} \quad (12)$$

where  $C_N^B(t - \Delta t)$  is the solute concentration at the grain boundary at the previous  $\Delta t$ .

The grain boundary segregation proceeds until the solute concentration at the grain boundary  $C_N$  attains the equilibrium concentration at the grain boundary  $C_{GB}^\infty(t)$ . However, desegregation occurs when  $C_{GB}^\infty(t) < C_N(t - \Delta t)$ . Desegregation

during the cooling stage was also calculated based on a one-dimensional diffusion model (see Fig. 10B). During the desegregation processes, it was assumed that solute diffusion also occurred in excess of the solubility limit of a solute element (i.e., supersaturation was permitted).

#### Analysis Conditions

The cosegregation behavior to the grain boundary was computed for P and S during the welding process. The material constants used for the numerical simulation are summarized in Table 2. The interaction parameter between P and S ( $-78.3$  kJ/mol) meant that the interaction was “repulsive (competitive)” during segregation. In the present simulation, the cooling rates during and after solidification were estimated as 300 and 150 K/s, respectively, based on the thermal cycle measured during actual welding. Nominal liquidus and solidus temperatures (solid-liquid coexistence temperature range) of the alloy were calculated using the phase computation software, *Thermo-Calc* (database: SSOL-4). The growth velocity of a dendrite was assumed to be 1.67 mm/s (identical to the welding speed). A dendritic cell (10  $\mu$ m in diameter) was divided into 100 segments. The FDM calculation of segregation and desegregation was conducted from the liquidus temperature to the room temperature through the solidus temperature.

#### Microsegregation to Grain Boundary during the Welding Process

A computer simulation of grain boundary segregation in P and S during

the weld cooling process was carried out for the weld metals U21–U25. Figure 11 shows the relation between the elapsed time in the welding thermal cycle and calculated P and S concentrations at grain boundaries for various initial P and S contents. During solidification, the P and S concentrations in the liquid phase increased with the progress of solidification, and very high amounts of P and S were segregated to grain boundaries at the solidification completion. The P and S concentrations were rapidly reduced to their equilibrium concentrations (desegregation) when the weld metal was cooled down; however, they increased gradually again at lower temperatures. The grain boundary concentration of S during welding was relatively higher than that of P even when their initial contents were comparable. This fact suggests that grain boundary segregation of S would become more pronounced compared with P during welding (probably related to the competition between P and S).

The effect of the initial contents of P and S in the weld metal on grain boundary segregation during welding was also investigated. The P and S concentrations in grain boundaries at 1643 K, which is the lower limit of the ductility-dip cracking temperature range, were computed for different initial P and S contents. Figure 12 shows the relationships between calculated P and S concentrations at grain boundaries and initial P and S contents in the weld metal. The P and S concentrations at grain boundaries linearly increased with an increase in their initial contents, and attained values approximately 40 and 240 times as high as their

initial contents, respectively. It follows that P and S are cosegregated to a grain boundary in the weld metal during welding, and that their segregated concentrations at grain boundaries are approximately proportional to their initial contents.

#### Grain Boundary Embrittlement Due to P and S Analyzed by the Molecular Orbital Method

The binding strength of the grain boundary was numerically analyzed by a molecular orbital analysis (DV- $X\alpha$  method (Ref. 18)). Figure 13 schematically illustrates the cluster model used in the present computation, the  $\Sigma 15$  coincidence boundary (simulating a high-angle grain boundary) of  $\gamma$ -Fe consisting of 67 atoms. One or two Fe atoms on a grain boundary were replaced by P or S atoms to simulate grain boundary segregation. The binding strength of a grain boundary was evaluated from the bond order between intergranular and intragranular Fe atoms in the near neighborhood of P and S atoms (it is known that the bond order is linearly correlated with the interatomic bond strength).

The calculated bond orders of the Fe atom at a grain boundary for different segregation situations are shown in Fig. 14. In this figure,  $Fe_{67}$  indicates the nonsegregated situation,  $Fe_{66}X_1$  and  $Fe_{65}X_2$ ,  $Fe_{65}X_1Y_1$  (X, Y = P, S) indicate the segregated situations where one and two intergranular Fe atoms were replaced by an X and/or Y atom, respectively. Thus, " $Fe_{65}X_2$ " as well as " $Fe_{65}X_1Y_1$ " means that grain boundary segregation has proceeded further compared to " $Fe_{66}X_1$ ," and furthermore " $Fe_{65}X_1Y_1$ " indicates the situation of P and S cosegregation.

When P and S were segregated at grain boundaries, the bond orders of the Fe atoms were reduced compared to the nonsegregated situation, and the bond orders decreased with an increase in the number of segregated P and S atoms. The bond orders of the Fe atoms when S was segregated to a grain boundary were lower than those for P segregation. However, the fact that the calculated bond order of an Fe atom in  $Fe_{65}P_1S_1$  ranked between those in  $Fe_{65}P_2$  and  $Fe_{65}S_2$  prevented the confirmation of any discernible effect of cosegregation with P with S in the present analysis.

#### Mechanism of Ductility-Dip Crack Generation

Here the authors discuss the mechanism of ductility-dip crack generation in extra-high-purity 25Cr-35Ni steels. A grain boundary segregation analysis revealed that P and S (especially S) were segregated to grain boundaries in the weld metal during welding. A molecular orbital analysis suggested that there was a possibility that grain

boundary segregation of P and S led to grain boundary embrittlement at the hot cracking temperature. A currently acceptable mechanism of ductility-dip cracking is attributed to an imbalance between intergranular strength and intragranular strength at a high temperature. Extra-high-purity 25Cr-35Ni steel maintains a superior intragranular strength, especially at an elevated temperature, a feature that originates in its high Cr and Ni content. On the other hand, grain boundary segregation of P and S leads to the deterioration of intergranular strength at higher temperatures during the welding process. Consequently, grain boundary segregation of P and S brings about the situation that intergranular strength falls below intragranular strength, and would accordingly promote grain boundary sliding at higher temperatures where the cracks are initiated. Such grain boundary sliding initiates a ductility-dip crack at a grain boundary.

On the other hand, the influence of S in increasing the ductility-dip cracking susceptibility was approximately 1.2 times as large as that of P — Fig. 8. The authors feel that the numerical analysis results, which indicate that the influence of S in promoting grain boundary segregation and embrittlement is larger than that of P — Figs. 12 and 14, are supported by this experimental fact. It follows that the ductility-dip cracking should be greatly inhibited by limiting the presence of S, as well as P, to very low amounts.

#### Improvement in Hot Cracking Susceptibility by La Addition

With the aim of applying this steel to more severe environments, the authors tried to further improve the hot cracking (ductility-dip cracking) susceptibility of extra-high-purity 25Cr-35Ni steel. From the fact that a principal cause of ductility-dip crack generation is probably grain boundary embrittlement attributed to grain boundary segregation of impurity elements such as P and S, the authors investigated the effect of La addition to the steel. According to a number of previous studies (Refs. 5, 19–23), REM such as La and cerium (Ce) possesses a high affinity for the impurity elements such as P and S, and has improved the hot cracking susceptibility of various steels and alloys. However, severe restrictions were additionally imposed on the proper additive amount of the REM. In the present study, the effect of La addition on the hot cracking susceptibility and optimal amount of La are investigated for extra-high-purity steels.

#### Evaluation of Hot Cracking Susceptibility by Transverse-Varestraint Test

The hot cracking susceptibility of extra-high-purity 25Cr-35Ni steels with

different amounts of La (U26-U28) added was evaluated by the transverse-Varestraint test. Figure 15 shows the effect of the amount of La added on the BTR and DTR of the steels. The DTR was reduced with an increase in the amount of La and was nearly saturated with over the approximately 50 ppm addition of La. In contrast, the BTR increased monotonically with an increase in the amount of La up to levels of more than approximately 80 ppm. Both the BTR and DTR remained at a low level for La additions between approximately 20–70 ppm in the present extra-high-purity 25Cr-35Ni steels containing 6–8 ppm P and S. These results suggest that the hot cracking susceptibility could be further improved by adding the optimal amount of La, even when P and S were refined to an extremely low level (extra-high-purity grade) in 25Cr-35Ni steel.

#### Microstructural Analysis of La-Containing Weld Metal

To clarify the mechanism of the improvement for the hot cracking susceptibility by La addition, microstructures of the La-containing weld metals were analyzed. Microscopic observation revealed that fine products were formed in the La-containing weld metals. These fine products were then identified by the extraction residue method. Figure 16 shows the X-ray diffraction patterns of extraction residues from weld metals U26–U28. La phosphide ( $LaP_2$ ) and La sulfide ( $LaS_2$ ) were identified in every weld metal. Furthermore, the Ni-La intermetallic compound ( $Ni_5La$ ) was additionally identified in the weld metal U28 (very-high La added to the steel) as shown in Fig. 17.

#### Mechanism of Improvement in Hot Cracking by the Addition of La

To further investigate the mechanism by which the hot cracking susceptibility of extra-high-purity 25Cr-35Ni steel was improved by the addition of La, the hot ductility of the La-containing weld metals was evaluated by the Gleeble® test. Average values of the reduction of area of the weld metals (U26–U28) within the ductility-dip temperature range are compared in Fig. 9. The hot ductility of the La-free weld metals was approximately 70%, while that of the La-containing weld metals attained values as high as approximately 100%. It follows that the hot ductility was obviously improved by the addition of La.

From the fact that La phosphide and sulfide were formed in the La-containing weld metals, the microsegregation of P and S to grain boundaries would be depressed, considering that La is known to scavenge P and S in the weld metal (Refs. 17, 20). Consequently, it can be deduced

that the ductility-dip cracking susceptibility would be improved by the amelioration of the hot ductility of the weld metal (promoting recovery from grain boundary weakening). On the other hand, excessive La addition to the steel leads to the opposite effect of solidification cracking in the weld metal. Such excessive La addition also leads to the formation of a Ni-La intermetallic compound in the weld metal, which has a low melting point (about 1543 K for Ni<sub>5</sub>La/Ni eutectic (Ref. 19)). Therefore, solidification cracks would occur in the weld metal at a very high La content as a result of the enlargement of the BTR (brittle temperature range between solidus and liquidus).

## Conclusions

In the present report, the hot cracking behavior of extra-high-purity 25Cr-35Ni steel was investigated, and quantitative influences of minor and impurity elements on the hot cracking susceptibility were clarified. Furthermore, the effect of La addition to the steel was investigated to further improve the hot cracking susceptibility of extra-high-purity stainless steels.

The results obtained may be summarized as follows:

1) Cracks occurring in the transverse-Varestraint test of extra-high-purity 25Cr-35Ni steels could be classified into solidification and ductility-dip cracks. The solidification cracking susceptibility remained at a usefully low level, while the ductility-dip cracking susceptibility exceeded that of Type 310EHP stainless steel when the P and S contents were high.

2) The DTR and BTR of extra-high-purity 25Cr-35Ni steel could be expressed by the compositional parameter of  $P + 1.22S$  and  $P + 1.19S$ , respectively. Namely, S essentially enhanced the ductility-dip and solidification cracking susceptibilities approximately 1.2 times as effectively as P. Furthermore, the amount of  $P + 1.22S$  in steels should be limited to approximately 90 ppm to obtain a sufficiently low hot cracking susceptibility in 25Cr-35Ni steel welds.

3) A grain boundary segregation analysis revealed that P and S (especially S) were segregated to grain boundaries in the weld metal during welding. A molecular orbital analysis suggested that there was a possibility that grain boundary segregation of P and S led to grain boundary embrittlement at the hot cracking temperature. It was deduced that ductility-dip cracking could be attributed to grain boundary embrittlement due to grain boundary segregation of P and S.

4) To further improve the hot cracking susceptibility of extra-high-purity 25Cr-35Ni steel, the effect of La addition on the hot cracking susceptibility was investigated. The solidification and ductility-dip cracking susceptibilities could be improved by adding 20–70 ppm La to the steel.

5) The ductility-dip cracking susceptibility decreased as a result of the desegregation of P and S to grain boundaries due to the scavenging effect of La. On the other hand, the solidification cracking susceptibility increased at higher La contents, a change attributed to the enlargement of the brittle temperature range between solidus and liquidus.

## Acknowledgments

The authors would like to thank K. Hata (Osaka University) for his cooperation in this research. The present study includes the result of Research and Development of Nitric Acid Resistant Material Technology Applicable to the Next Generation of Reprocessing Equipment awarded to Kobe Steel, Ltd., by the Ministry of Education, Culture, Sports, Science and Technology of Japan (MEXT).

## References

1. Inazumi, T., Hyakubu, T., Takagi, Y., Okimoto, S., Ehira, Y., and Ohashi, M. 1993. Development of highly corrosion resistant R-SUS304ULC for nuclear fuel reprocessing plant. *NKK Technical Report* 144: 20–25 (in Japanese).
2. Nakayama, J., Noura, T., Yamada, H., and Yamamoto, K. 2009. extra-high purity alloy EHP for next generation nuclear systems. *Kobe Steel Eng. Rept.* 59(2): 94–97 (in Japanese).
3. Kiuchi, K., and Ioka, K. 2009. Development of extra-high purity stainless steels for next generation nuclear systems. *Genshiryokue* 55(5): 54–58 (in Japanese).
4. Nishimoto, K., Saida, K., Okabe, Y., Hata, K., Kiuchi, K., and Nakayama, J. 2010. Hot cracking behaviour and susceptibility of extra-high-purity Type 310 stainless steels. *Sci. & Technol. Welding & Joining* 15(1): 87–96.
5. Matsuda, F., Nakagawa, H., Katayama, S., and Arata, Y. 1982. Weld metal cracking and improvement of 25%Cr-20%Ni (AISI310S) fully austenitic stainless steel. *Trans. JWS* 13(2): 115–132.
6. Ogawa, T., and Tsunetomi, E. 1982. Hot cracking susceptibility of austenitic stainless steels. *Welding Journal* 61(3): 82-s to 93-s.
7. Kujanpää, V. P., David, S. A., and White, C. L. 1986. Formation of hot cracks in austenitic stainless steel welds — solidification cracking. *Welding Journal* 65(8): 203-s to 212-s.
8. Kujanpää, V. P. 1985. Effect of steel type and impurities in solidification cracking of austenitic stainless steel welds. *Metal Construc-*

*tion* 17(1): 40R to 46R.

9. Rabensteiner, G., Tosch, J., and Schabereiter, H. 1983. Hot cracking problems in different fully austenitic weld metals. *Welding Journal* 62(1): 21-s to 27-s.

10. Lundin, C. D., Chou, C. – P. D., and Sullivan, C. J. 1980. Hot cracking resistance of austenitic stainless steel weld metals. *Welding Journal* 59(8): 226-s to 232-s.

11. Gooch, T. G., and Honeycombe, J. 1980. Welding variables and microfissuring in austenitic stainless steel weld metal. *Welding Journal* 59(8): 233-s to 241-s.

12. Li, L., and Messler, Jr., R. W. 1999. The effect of phosphorus and sulfur on susceptibility to weld hot cracking in austenitic stainless steels. *Welding Journal* 78(12): 387-s to 396-s.

13. Homma, H., Nishi, T., and Kohira, K. 1980. Application of the Tigamajig test to the study of hot-cracking in weldments. *J. JWS* 49(5): 290–296 (in Japanese).

14. Saito, K., Aoki, M., Mineura, K., Kondo, H., and Ikeda, N. 1985. The effect of phosphorus content on weld hot cracking of Alloy 800. *Nippon Stainless Tech. Rept.* No. 20: 17–43 (in Japanese).

15. Saito, K., Aoki, M., Kondo, H., and Ikeda, N. 1988. Influence of boron content on hot cracking sensitivity of weld heat-affected zone in Alloy 800. *Nippon Stainless Tech. Rept.* No. 23: 35–51 (in Japanese).

16. Saida, K., Nomoto, Y., Taniguchi, A., Sakamoto, M., and Nishimoto, K. 2010. Microcracking behaviour and mechanism in multipass weld metal of Alloy 690. *Quar. J. JWS* 28(1): 61–71 (in Japanese).

17. Xu, T. 1987. Non-equilibrium grain-boundary segregation kinetics. *J. Mater. Sci.* 22(1): 337–345.

18. Adachi, H. 1998. Hajimete-no-Densijotai Keisan. Sankyo Publishing (in Japanese).

19. Nishimoto, K., Saida, K., Okaguchi, H., and Ohta, K. 2006. Prevention of microcracking in reheated weld metal by La addition to filler metal — Microcracking in multipass weld metal of Alloy 690 (Part 3). *Sci. & Technol. Welding & Joining* 11(4): 471–479.

20. Saida, K., Taniguchi, A., Sakamoto, M., and Nishimoto, K. 2009. Effect of Ce addition to filler metal on microcracking susceptibility of Alloy 690 multipass weld metal. *Quarterly Journal of the Japan Welding Society* 27(2): 144-s to 148-s.

21. Nishimoto, K., Woo, I., and Shirai, M. 2002. Underlying mechanism in the improvement of HAZ cracking susceptibility by rare earth metal addition — Study on weldability of cast Alloy 718 (Report 8). *Quar. J. JWS* 20(1): 87–95 (in Japanese).

22. Nishimoto, K., Saida, K., and Fujiya, Y. 2009. Amelioration of micro-cracking in multipass weld metal of Alloy 690 by adding rare earth metals. *Proceedings of PVP2009 (ASME Pressure Vessels and Piping Division Conference)*, PVP2009-77235.

23. Nakao, Y., and Katsu, S. 1986. Improvement of solidification cracking susceptibility of electron beam weld metal of fully austenitic Type 316 stainless steel. *Quar. J. JWS* 4(2): 393–399 (in Japanese).